Cation-heterogeneity in internally gelated $U_{1-z}Ce_zO_{2-x}$, $0.15 \leq z \leq 0.3$ microspheres

Authors and affiliations

Selim Uygur[1,2], Rémi Delville[1], Christian Schreinemachers[3], Gregory Leinders[1], Nico Vanhove[1], Wouter Van Renterghem[1], Marc Verwerft[1], Jozef Vleugels[2]

[1] Belgian Nuclear Research Centre (SCK-CEN), Institute for Nuclear Energy Technology, 2400 Mol, Belgium
[2] KU Leuven, Department of Materials Engineering (MTM), Kasteelpark Arenberg 44/bus 2450, 3001 Leuven, Belgium
[3] Forschungszentrum Jülich GmbH, Institute of Energy and Climate Research, IEK-6: Nuclear Waste Management, 52425 Jülich, Germany
E-mail of corresponding author: selim.uygur@student.kuleuven.be

Highlights

- Microstructure of internally gelated microspheres (IGMS) was studied.
- Cross-sections of $(U,Ce)O_2$ IGMS with varying Ce content were mapped for U, Ce.
- XRD peak anomalies in IGMS were clearly linked to U/Ce distribution heterogeneity.
- Implications of silicon trace presence on the IGMS microstructure was discovered.
- Ce-rich precipitates were characterized to be non-fcc $Ce_{4.67}(SiO_4)_3O$ single grains.

Abstract

Internal gelation of aqueous mixtures of metal (M = *Ln*, *An*) nitrate with Uranyl Nitrate is generally assumed to yield cation homogeneity and a fluorite type single phase $U_{1-z}M_zO_{2\pm x}$ solid solution. As-sintered $(U,Ce)O_2$ internally gelated microspheres, manufactured with target z values up to 0.3 using $Ce(NO_3)_3$, were observed to exhibit systematic peak broadening and splitting at higher 2θ angles in their X-Ray diffraction (XRD) patterns, correlating with increasing z≥0.15. This was interpreted as an unexpected departure from a single phase material. Thermogravimetry was used to make an initial assessment whether these peak anomalies where caused by an oxygen hypostoichiometry. Results indicated global oxygen stoichiometry for all compositions. The subsequent detailed characterization study via Electron Probe Micro Analysis of cross-sections of the as-sintered microspheres revealed the systematic presence of spherical Ce concentration gradients, as well as µm-sized highly Ce-enriched features. EDS and TEM studies on focused ion beam lamellae extracted from the cross-sections of as-sintered microspheres revealed a hexagonal $Ce_{4.67}(SiO_4)_3O$ minor phase manifesting as single grain precipitates and clusters uncovering the presence and critical role of Silicon as an unexpected contaminant and Ce-scavenger from surrounding $(U,Ce)O_2$ grains. Characterization at intermediate heat treatment steps revealed that the systematic U/Ce heterogeneity features are already present post-gelation and are independent of the superimposed trace Ce-Si-O phase. This work constitutes the first systematic cation distribution study on cross-sections of $(U,Ce)O_{2\pm x}$ microspheres, executed on a series of compositions, using a combination of elemental mapping techniques.

Keywords: Cerium, Uranium, Mixed oxides, Homogeneity, Internal Gelation, Elemental mapping

1. Introduction

The sol-gel process has been investigated for several decades as an alternative route to produce actinide bearing nuclear fuel without generating radiotoxic dust. The term sol-gel describes a class of solution based routes to produce ceramic nuclear fuels. A sol describes an aqueous (mixed) metal nitrate solution, possessing the desired final molar metal fractions, and in most cases also process-specific chemicals, in particular gelation agents. Microspheres of a few tens to a few hundred micrometer in diameter can be obtained within a domain of synthesis parameters [1], [2] which are

generally based on the reaction of the sol, with gaseous and/or liquid ammonia. Hydrolysis into insoluble often hydroxide compounds takes place under conditions of a rapid pH increase, and solid spherical particles form. This step is called gelation. Sol-gel methods are generally categorized into internal and external gelation [3]The fundamental difference between them is how the ammonia is introduced into the system. For the case of external gelation[1], sol droplets are first dripped from a nozzle through a volume of gaseous ammonia before being immersed into a bath of aqueous ammonia solution. The droplets become shaped as spheroids upon falling from the nozzle. The ammonia is introduced from the outside via a gas/liquid interface to trigger the gelation. The contact between gaseous ammonia and liquid droplets enables solidification of the outer surface, which helps to maintain the spherical shape upon hitting the liquid surface interface. For internal gelation (IG)[4], urea and hexamethylenetetramine (HMTA) are present in the sol. Those so-called gelation agents decompose when they are exposed to heat and form ammonia which triggers the solidification.

The application of the sol-gel route on mixed aqueous solutions of uranyl nitrate and lanthanide- or actinide-nitrate allow to obtain solid, spherical precursor agglomerates without the generation of dust. Those precursor materials can be thermally processed in order to obtain the desired properties. One of the most common applications being the production of mixed oxide microspheres. This is particularly of interest for preparing Pu and minor actinide (MA) bearing fuel materials to prevent the creation of MA containing dust. Microspheres can also be dosed rather easily and are well suited for automated continuous fuel production forms; i.e. pelletization, vibro-packing, or TRISO type (pebble) fuel[5]–[8]. Sol-gel processes have been demonstrated extensively on lanthanide (*Ln*)/actinide(*Ac*) doped uranium mixed oxide systems, and have been reported to result in homogeneous solid solutions of Uranium (U) with Neodymium (Nd)[9], [10], Cerium (Ce) [11], Gadolinium (Gd) [12], Thorium(Th) [13], Neptunium (Np) [14], Plutonium (Pu) [15], and others[2]. Lanthanides are often used as surrogates for actinides to perform feasibility studies and explore process parameters without the need for shielded facilities.

Ce mimics many properties of Pu in particular in the tetravalent state, which is prevalent for O/*M* ratios that are of interest to study mixed oxide (MOX) materials. The ionic radii of Ce^{4+} and Pu^{4+} in an 8-fold coordinated environment are similar (0.96 Å and 0.97 Å, respectively [16]), but differ more significantly for Ce^{3+} and Pu^{3+} in a 9-fold coordinated environment (1.168 Å and 1.191 Å, respectively [16]). In the range between ambient temperature and commonly applied sintering temperatures (1473 K to 1973 K), the U-Ce-O phase system is mimicking the U-Pu-O system remarkably well in the composition range UO_2-MO_2-M_2O_3, with *M*={Pu, Ce}, and partly in the higher oxide domain. Some differences in regard to the domain boundaries of the miscibility gap and the nature of additional phases at the edges thereof exist [17]–[23].

The manufacturing of $U_{1-z}Ce_zO_{2\pm x}$ internally gelated microspheres (IGMS) was recently investigated by Schreinemachers et al. [24] and ambient X-Ray powder diffraction (XRD) patterns of the products indicated the presence of a single face-centered cubic, fcc (Fm-3m), phase for compositions with Ce molar metal fractions of 5 mol%, 10 mol% and 15 mol%. Patterns of compositions with 20 mol%, 25 mol% and 30 mol% Ce exhibited asymmetric peak broadening and peak splitting at higher 2θ angles [24]. This was interpreted as the existence of multiple phases [24].

Asymmetric peak broadening and/or peak splitting could indeed be caused by the formation of more than one fcc phase with distinct Ce content but also by a non-uniform distribution of Ce across the IGMS. Additionally, an oxygen-driven miscibility gap, known to occur for $x < 0$ and $z \geq$ ~0.3 during cooling down after sintering [17], [25], results in the formation of two fcc phases $U_{1-z}Ce_zO_{2.00}$ and $U_{1-z}Ce_zO_{2-x}$. Further characterization is required in order to investigate the origin of the separation, in particular the Ce distribution in the particles. For $U_{1-z}Ce_zO_{2.00}$ microspheres obtained via external

gelation, at least one study reports cation homogeneity via a combined effort of XRD and an Electron Probe Micro Analysis (EPMA) mapping of Ce on a limited cross-section area[5]. To the best of our knowledge, the application of location sensitive techniques on $U_{1-z}Ce_zO_{2.00}$ IGMS has not been reported in open literature [1].

In this work, the nature and origin of the departure from a single phase material in the XRD patterns of as-sintered $U_{1-z}Ce_zO_{2.00}$ IGMS were investigated. The Ce-doped IGMS, that were already manufactured for the previous study in which XRD peak shape anomalies were reported, and where not yet thermally treated, were subjected to new thermal treatment. Along the treatment steps the global as-sintered O/*M* ratios were measured for each composition, and, in combination with ambient XRD after each thermal treatment, a comprehensive elemental analysis of the cation distribution on entire cross-sections of internally gelated microspheres, over a range of Ce-dopant compositions was carried out.

2. Experimental

2.1. Material

2.1.1. Microsphere fabrication

The Ce-doped uranium oxide microspheres studied within this work contain Ce molar metal fractions of up to 30 mol% and were fabricated by the sol-gel route via IG. They consist of a remaining stock of dried microspheres produced and reported by Schreinemachers et al. [24].

Acid-deficient uranyl nitrate (ADUN) solution and cerium(III) nitrate hexahydrate solution acted as metal precursor solutions. Certain volumes were mixed and a solution containing the gelation agents urea and HMTA was added. Details of the precursor are described in [24]. The resulting solution represents the sol, which had a total metal concentration of 1.3 mol/L. The amount of gelation agent is commonly expressed as ratio of their molar amount over the molar metal amount, which was 1.2 for both gelation agents, urea and HMTA. Polydimethylsiloxane (PDMS), a silicone oil, tempered to 363 K acted as heat transfer medium and droplets of the sol were added in order to obtain spherical particles. Afterwards, the microspheres were retrieved from the oil, washed, aged in ammonia solution, and dried. A fraction of the products of each batch was dissolved in HNO_3 and the metal contents in the resulting solution were analyzed by inductively coupled plasma mass spectrometry (ICP-MS) to determine the actual Ce molar metal fractions, which are listed in Table 1. For simplicity $\chi(Ce)_{aimed}$ values are referenced to within the manuscript. Comprehensive experimental details on the preparation conditions are available in [24].

Table 1: Ce molar metal fractions of nominal compositions $\chi(Ce)_{aimed}$ studied in this work and those determined via ICP-MS analyses on dissolved as-dried IGMS, $\chi(Ce)_{analyzed}$ [24].

$\chi(Ce)_{aimed}$	$\chi(Ce)_{analyzed}$
[mol%]	*[mol%]*
5	5.1(7)
10	10(1)
15	16(2)
20	21(3)
25	25(3)
30	31(3)

2.1.2. Thermal treatment

A thermal treatment of the dried material was carried out using the conditions and equipment mentioned in [24]. The general treatment consisted of two individual steps: (I) calcination in air and (II) sintering in a reducing environment.

For the first treatment step, dried microspheres of each batch were transferred into alumina crucibles and heated at 1.5 K min^{-1} to 1173K in air (furnace: Nabertherm, LT 9113/P330). After a dwell time of 1 h, the samples were allowed to cool to 298 K. The calcined material was subsequently sintered in custom made Mo-crucibles (furnace: Linn High Therm, HT-1800-Moly) under a reducing atmosphere consisting of Ar:4%H_2 and Ar:0.5%O_2 with respective flow rates of 1428 mL/min and 72 mL/min and resulting in a μO_2 of about -420 kJ/mol at the sintering temperature. The thermal profile consisted of: Heating to 973 K in Ar at 5K/min, switching to the sintering atmosphere and holding for 1.5 h at 973 K. Subsequently, the temperature was increased to 1873 K at a heating rate of 5K/min and was held for 10 h. At the end of the sintering isotherm the atmosphere was switched again to Ar at a flow rate of 1500 mL/min and the furnace cooled down at 5 K/min to 473 K. This replicated the treatment reported in [24]. The cooling to ambient temperature took place in an inert atmosphere. The products of this treatment are referred to in this study with the term *main series*.

2.2. Characterization

2.2.1. Determination of O/*M* ratios

In order to determine the actual oxygen content for all compositions in the as-sintered state, the oxygen to metal ratio (O/M) was determined by thermogravimetry (TG). This type of analysis is commonly described with the term equilibration, which we use in this study as well. A Setaram Setsys 1750 CS Evolution simultaneous thermal analyzer (STA) was used to perform the analyses on the sintered $U_{1-z}Ce_zO_{2+x}$ microspheres. Conditions resulting in an exact O/M ratio of 2.00 in the sample material were applied. The recorded mass difference was attributed to oxygen uptake or release, allowing to calculate the oxygen content of the material prior to the analysis. Initial *ex-situ* sample masses, which ranged from 320 mg to 470 mg, were weighed into an Al_2O_3 crucible ($V_{crucible}$ = 1.3 mL) using a Mettler-Toledo AT201 precision balance with an uncertainty of ± 0.14 mg (2σ). The crucible was hooked to the STA via platinum wires and a comparability of the individual measurements was guaranteed by maintaining a furnace temperature of 313 K for 30 min prior to the equilibration. The mass present at the end of this stabilization plateau is considered as initial *in-situ* mass. Afterwards, the furnace chamber was purged to a pressure of $p \leq$ 5E-2 mbar and Ar was introduced with a flow rate of 200 mL min^{-1} for 10 min. This procedure was carried out twice. Then, the atmosphere was changed to correspond to an oxygen potential $\mu(O_2)$ of -376 kJ mol^{-1} at 1073 K which is based on thermodynamic data of the ternary system U-Ce-O [18], [19], [26], obtained using Ar:H_2 (96:4) and Ar:O_2 (99.5:0.5) gas mixtures with flow rates of 26 mL min^{-1} and 54 mL min^{-1} respectively. For the undoped $UO_{2\pm x}$ composition flow rates of 60 mL min^{-1} and 20 mL min^{-1} corresponding to an oxygen potential of about -420 kJ mol^{-1} at 1073 K [27], were used. The sample material is equilibrated at a temperature of 1073 K for 12 h, which is reached by applying a heating rate of 10 K min^{-1}. After 12 h the atmosphere was switched to Ar, which was kept for another 30 min. Then, it was cooled down to 313 K at a rate of 10 K min^{-1}. At 313 K, a final isotherm of 60 min was maintained. Afterwards, the final *ex-situ* mass was measured, using the Mettler-Toledo AT201 precision balance. The mass at the end of each equilibration isotherm ($\mu(O_2)$ of -376 kJ mol^{-1} or -420 kJ mol^{-1}) was subtracted from the initial *in-situ* mass in order to determine the mass difference obtained during the equilibration. It corresponds to the deficiency or excess of oxygen as compared to the ideal stoichiometric MO_2 composition with an O/*M* ratio of 2.00, and thus yielded the O/M ratio of the IGMS in the as-sintered state.

2.2.2. XRD measurements

At the end of each thermal treatment step, calcination, sintering and equilibration respectively, a small amount of IGMS was set aside from each batch and stored in 2 mL gas-tight glass vials for subsequent XRD measurements. For each XRD measurement these stored particles were crushed in an agate mortar with an agate pestle just before measurement. The resulting powder was dispersed on a silicon zero-background sample holder. A Bruker Advance D8 diffractometer, with a Lynx-Eye detector and a Cu anode emitting a beam wavelength $\lambda(Cu\ K_{\alpha 1})$= 1.5405929 Å [28] was used with a voltage of 40 kV and a current of 40 mA. The instrument was mounted with a soller slit assembly having 2.5° axial divergence, and a Ni beam mask to attenuate Cu K_{β}. Instrument alignment was validated prior measurements using a sintered alumina disc (NIST Standard Reference Material 1976B). The position sensitive detector window was set to the maximum of 3.288°. A step size of 0.015° 2θ with time per step values varying between 0.3 s and 0.6 s per step were configured. The sample holder rotated continuously at 15 rpm. Native DIFFRAC.EVA Commander, Version 7.3.1, was used as data acquisition software. Depending on the measurement purpose, several acquisition ranges were used between 15° and 145° 2θ.

Diffraction data analysis was executed using Panalytical Highscore X'pert v4.8 (Highscore) software. For all samples for which evidence of departure from single phase composition was present, i.e. pronounced peak asymmetry and/or broadening as well as the appearance of distinguishable peak separation, Rietveld refinement was employed to evaluate lattice parameters (LP) and phase compositions. For all other samples the more simple unit cell refinement function was used based on peak positions and on $\lambda(Cu\ K_{\alpha 1})$ only, implementing the method described by Nelson and Riley [29]. In both cases corrections for sample displacement were performed. Results were deemed satisfactory based on a figure of merit (FOM) calculated according to Jenkins and Schreiner[30].

Finally, a temperature correction was applied on all lattice parameters using the thermal expansion coefficient of UO_2 published by Fink et al. [31] at T_{ref} of 293 K and an average ΔT of 2.5 K. The temperature was measured twice throughout the acquisition campaign and assumed to be practically constant at 295.65 K. The thermal expansion coefficients of $(U,Ce)O_2$ diverge from pure UO_2 at high T and with increasing χ(Ce), but at and around $T_{ambient}$, e.g. 298 K, the coefficients for $(U,Ce)O_2$ for all χ(Ce) remain practically coincident with those of UO_2 [32].

2.2.3. Microstructural analysis

Selected compositions of the as-dried particles were analyzed via Scanning Electron Microscopy / Energy Dispersive Spectroscopy (SEM/EDS) in order to reveal microstructural features. In the case of the sintered and equilibrated particles, selected compositions were primarily investigated by EPMA while SEM/EDS was also used in some cases.

As dried and thermally treated particles of batches of interest (30-50 particles) were mixed with silver nano-powder (Alfa Aesar, 41599 Silver powder, spherical, APS 1.3-3.2 micron, 99.9 % (metals basis) CAS#:7440-22-4) and pressed into pellets (diameter: 8 mm, height: 6 mm–10 mm). Each pellet was embedded in Struers *polyfast* conductive hot mounting resin and subjected to mirror polishing. The microspheres were polished to about half of their diameter to reveal their cross-section.

The polished pellets containing dried particles were analyzed by Scanning Electron Microscope/Energy Dispersive X-ray spectroscopy (SEM/EDS). Measurements were carried out using a Jeol JSM 7100FA field-emission microscope, equipped with a secondary and backscattered electron detector. An accelerating voltage between 10 kV and 20 kV with beam current of 1-2 nA was employed. The working distance ranged from 7 mm to 10 mm. Elemental mappings of U, Ce and O were taken of the cross-

sections of the as-dried particles. Si was added in some re-measured samples after the discovery of the Si-presence in the as-sintered/as-equilibrated stages of the material. The raw maps were quantified using the P/B-ZAF method with background correction, part of the native JEOL software package.

Samples of the thermally treated particles were characterized by EPMA (Cameca SX100R) at ambient temperature under vacuum. Wavelength Dispersive Spectrometer (WDS) crystals used for O and Ce/U detection were PC1 and PET, respectively. Three types of analyses were performed: 1. Elemental mappings on entire cross-sections; 2. Quantitative elemental mappings of regions of interest (ROI) at high magnifications, and; 3. Quantitative line scans. These were conducted with beam currents ranging from 100 nA to 200 nA and a beam voltage of 10 kV to 20 kV.

In both types, quantitative elemental analyses were performed with a decreased beam voltage of 10 kV. Calibration of U and O were done using a UO_2 standard while a CeO_2 standard was considered for Ce. The M_α, K_α, L_α transitions were considered for the quantification of U, O and Ce, respectively.

2.2.4. Transmission Electron Microscopy (TEM) on Focused Ion Beam lamellae

During this work it became necessary to investigate the microstructure on a smaller scale at higher resolution than EPMA was able to offer. For this, samples were prepared for TEM analysis with a ThermoFisher Scios Focused Ion Beam/Scanning Electron Microscope (FIB/SEM) on an as-sintered and on an as-equilibrated 25 mol% Ce microsphere, respectively. Two lamellae were extracted from the edge of the as-sintered particles where high incidence of Ce-rich features was observed. One lamella was extracted close to the surface of an as-equilibrated particle and one was extracted from the interior of it. The extracted lamellae were welded on a copper grid by Pt deposition and thinned until electron transparency. The grids were mounted in a JEOL GrandARM 300F2 scanning transmission electron microscope operating at 300 kV and equipped with a JEOL DUAL DRY SD 320 EDS system. The location and composition of the different phases were determined from EDS element maps. To probe the local composition of the phases, a spectrum was extracted from the element map, by selecting a number of points from the same phase and summing all point spectra. The sum spectrum was quantified using the peak ratio method including an absorption correction. As the exact sample thickness was not determined a standard thickness of 150 nm was taken. To determine the crystallographic structure of the different phase(s), conventional bright field images and selected area electron diffraction patterns were recorded and analyzed.

3. Results

3.1. XRD Measurements

XRD patterns of as-calcined, as-sintered and as-equilibrated IGMS were recorded ranging from 20° to 145° 2θ with a step size of 0.3 s per step, as described in section 2.2.2. All patterns obtained on as-sintered and as-equilibrated samples of composition with Ce metal fractions of 0 mol%, 5 mol%, 10 mol% exhibit sharp and symmetric fcc reflections over the entire 2θ range, consistent with formation of a single fcc phase within the sensitivity of the measurement. However, compositions with Ce metal fractions above 15 mol% exhibited asymmetric peak broadening developing into peak splitting with increasing Ce content, suggesting the existence of multiple phases. Lattice parameters obtained from unit cell refinements for compositions exhibiting no peak shape anomalies are tabulated in Table 2, the lattice parameters calculated by Schreinemachers et al [24] are included as well. Both datasets agree well, showing a good reproducibility.

Table 2: Comparison and summary of temperature corrected lattice parameters from unit cell refinements in this work and in previous work[24]*; [(a)] Asymmetric peak shoulder towards lower angles in as-sintered 15 mol% composition observed.*

Metal nitrate precursor	$\chi(Ce)_{nominal}$ [mol%]	Phase separation reported in reference work	**As-sintered IGMS (Schreinemachers et al. 2020)**		Phase separation observed in this work	**As-sintered IGMS (this work)**			**As-equilibrated IGMS (this work)**		
			a (Å)	**$2\sigma_a$ (Å)**		***FOM***	**a (Å)**	**$2\sigma_a$ (Å)**	***FOM***	**a (Å)**	**$2\sigma_a$ (Å)**
ADUN	N/A	N/A	**5.4710**	0.0002	N/A	640	**5.4707**	0.0002	244	**5.4706**	0.0002
ADUN	5	NO	**5.4676**	0.0002	NO	983	**5.4675**	0.0002	813	**5.4673**	0.0002
+	10	NO	**5.4645**	0.0002	NO	228	**5.4647**	0.0002	589	**5.4643**	0.0002
Ce(III)	15	NO	**5.4613**	0.0002	**YES**[(a)]	623	**5.4614**	0.0002	980	**5.4608**	0.0002

The as-calcined samples yielded, as expected, orthorhombic and hexagonal patterns matching with U_3O_8, and Fm-3m fcc patterns matching well with CeO_2.

3.2. O/*M* measurement results

To investigate the global O/*M* ratio of each as-sintered IGMS batch, material was subjected to an equilibration treatment as described in 2.2.1. Well-established literature on thermodynamic equilibria of $(U,Ce)O_{2.00}$ indicates that annealing the samples under a reducing atmosphere of $\mu(O_2)$=-376 kJ/mol at 1073 K should result in a global O/*M* = 2.000 for compositions from 5 mol% up to 40 mol% Ce. This is irrespective of any minor local χ(Ce) variation so long they stayed within the range of validity.

Table 3: As-sintered O/M ratios for each studied IGMS composition, given as $\chi(Ce)_{analyzed}$, calculated based on TG measurement results via equilibration treatment in an STA. Calculated uncertainty δ is given as (2σ). Calculation is based on in-situ mass change, compared to expected O/M ratios in reference to established literature, under assumption of elemental purity and adherence to the treatment validity range of 5 mol% <χ(Ce) ≤ 40 mol%. In addition, indication is given whether deviation from single-phase fcc behavior was reported in previous[24] *and/or observed in present work.*

Metal nitrate precursor	$\chi(Ce)_{analyzed}$ [mol%]	Phase separation reported in previous work [(b)]	Phase separation observed in this work	STA results this work	
				O/M[(a)]	δ (2σ)
ADUN	N/A	N/A	N/A	1.999	0.002
ADUN + Ce(III)	5.1(7)	NO	NO	1.998	0.002
	10(1)	NO	NO	2.000	0.000
	16(2)	NO	**YES**[(c)]	1.998	0.002
	21(3)	**YES**	**YES**	1.998	0.001
	25(3)	**YES**	**YES**	2.002	0.001
	31(3)	**YES**	**YES**	1.997	0.001

(a) As-sintered, calculated from as-equilibrated O/M=2.000.
(b) Based on XRD patterns[24].
(c) Asymmetric peak broadening observed in XRD patterns in the as-sintered and as-equilibrated states. Visible amount of Ce-rich phase observed via EPMA.

For all batches stable masses were observed some hours before the end of the equilibration isotherm. Therefore, it was concluded that global thermodynamic equilibria were reached for the material under the conditions applied. The resulting O/*M* ratios are tabulated in Table 3. All stated results contain uncertainties covering a 95 % confidence interval (2σ). The results indicate that the global O/*M* ratio of the as-sintered IGMS corresponds to an ideal stoichiometric composition for all Ce contents. While this is in line with established literature for UO_2, it diverged from the expected ratios for the Ce doped batches under the applied sintering conditions.

The results indicate that phase separation based on an oxygen-driven miscibility gap can be ruled out, as the global O/*M* values are at, or very close to stoichiometry. However, it should be taken into account that the selected equilibration conditions are only valid for Ce contents up to 40 mol%. In case

of local heterogeneities where χ(Ce) values are outside the validity range, the obtained global O/*M* ratios cannot be correctly interpreted. Before concluding on the possible separation of a secondary phase, local microstructural analysis needs to be carried out to characterize the cation distribution in greater detail.

3.3. Cation distribution in IGMS

The first step to probe the crystallographic makeup of the as-sintered and as-equilibrated materials was to perform ambient XRD on ground IGMS. Figure 1 shows select reflections, here hkl=026, resulting from each studied fcc $(U,Ce)O_{2\pm x}$ composition for both states. The most significant observation is a systematically deviating peak shape at higher 2θ angles with increasing Ce contents. This is a further hint that the crystalline structure of the material is most likely inhomogeneous. Moreover, no significant peak shift was observed prior to and after equilibration, which is consistent with the TG results. In order to understand the nature of these XRD results, position and element sensitive EPMA was performed on polished cross-sections of the particles from each batch. To minimize the potential effect of deviation from a global O/*M* ratio of 2.00, mainly material in the as-equilibrated state was investigated by EPMA. The resulting elemental Ce mapping of the corresponding particles in the as-equilibrated state, are shown at the bottom in Figure 1.

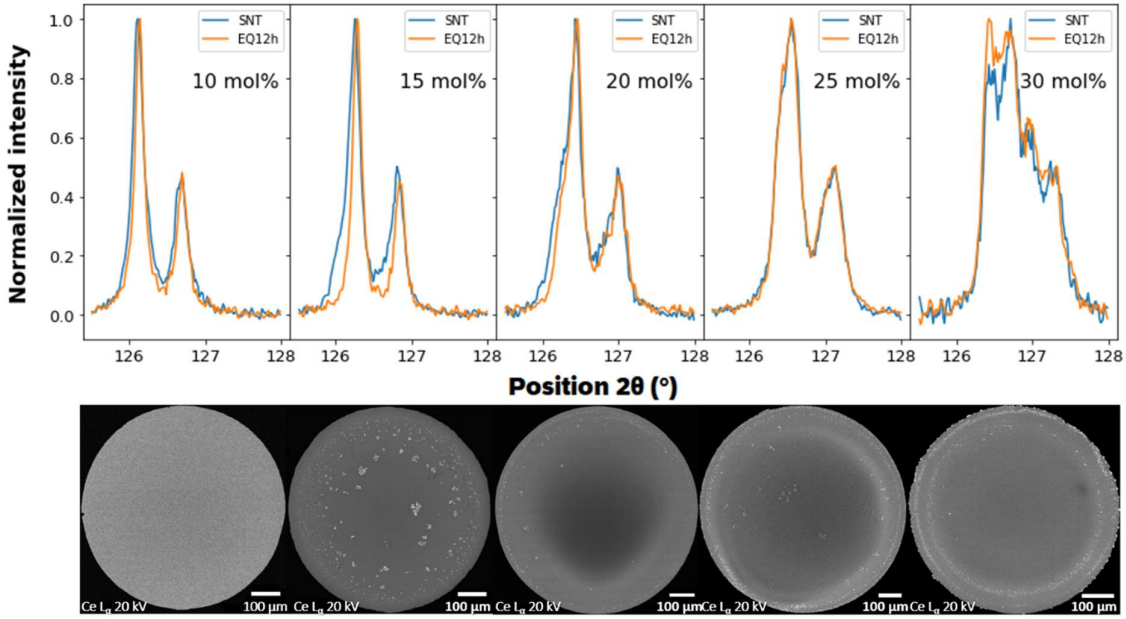

Figure 1: ***Top****: Normalized XRD reflections (hkl=026) of as-sintered (blue) and as-equilibrated (orange) IGMS;* ***Bottom****: EPMA Ce elemental maps of as-equilibrated IGMS cross-sections with χ(Ce)={10 mol%, 15 mol%, 20 mol%, 25 mol% and 30 mol%} from left to right).*

Heterogeneities in the Ce distribution are visually observable in elemental mappings of compositions with Ce content ≥ 15 mol%, which correlates to the asymmetry of the XRD reflections with increasing Ce content.

Figure 2 displays in greater detail the cation distribution in the cross-section of the 25 mol% Ce containing material. It contains features found in other samples as well and is characterized by a macroscopic radial gradient following a spherical ring-like pattern. The concentric Ce-enriched annular patterns are located toward the outer periphery while the center of the IGMS contains a region with more depleted and less fluctuating Ce content. Another recurring observation is the systematic presence of micrometer-sized precipitates (Figure 2c to 2e) with high Ce-content of up to 90 mol%.

The concentric gradients and precipitate-like features were analyzed via quantitative line scans across the IGMS cross-sections' diameter. Although the precipitates and precipitate clusters are also observed in more isolated random locations, a marked correlation of occurrence between the "wave-tops" on the radial Ce-gradient and the increased prevalence of the precipitates was observed.

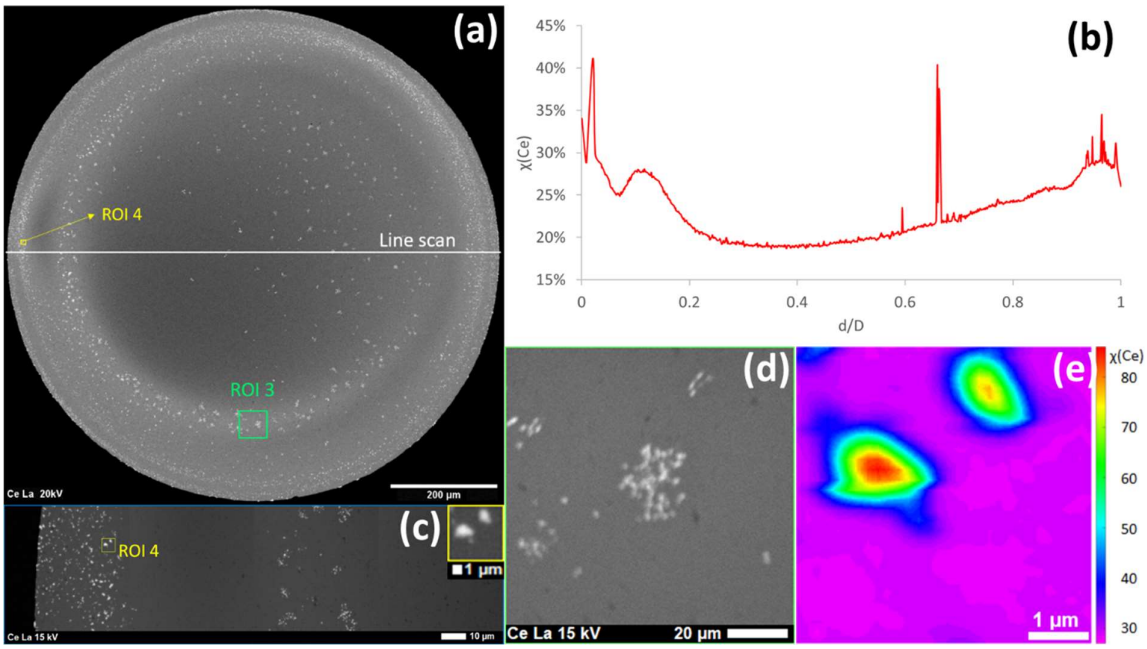

Figure 2: (a) Ce-mapping via EPMA of the cross-section of an equilibrated IGMS with χ(Ce)= 25 mol%, (b) Line scan on the diameter, (c) Zoom to location of ROI4 with Ce-rich precipitates, (d) ROI3 Ce-map: Ce-rich precipitate cluster, (e) Quantified elemental map of Ce in ROI4 given in χ(Ce).

3.4. Silicon presence

Given the thermodynamic quasi-equilibrium established during the thermal treatment, the high local Ce content measured for the precipitates could not be explained within the well-established fcc domain of the U-Ce-O diagram. Furthermore, quantitative EPMA measurements revealed non-negligible missing mass at locations that were highly Ce-enriched. A systematic EPMA wave scan on the samples' cross-section showed a co-occurrence of high Ce contents and small amounts of Si. Following this unexpected discovery some of the previously investigated samples were re-mapped including Si analysis. Moreover, samples of different fabrication states were investigated. The Ce and Si EPMA mappings of two IGMS in the as-sintered and as-equilibrated state are depicted in Figure 3. The latter shows a 1:1 spatial correlation between locally present Si and the enriched Ce regions.

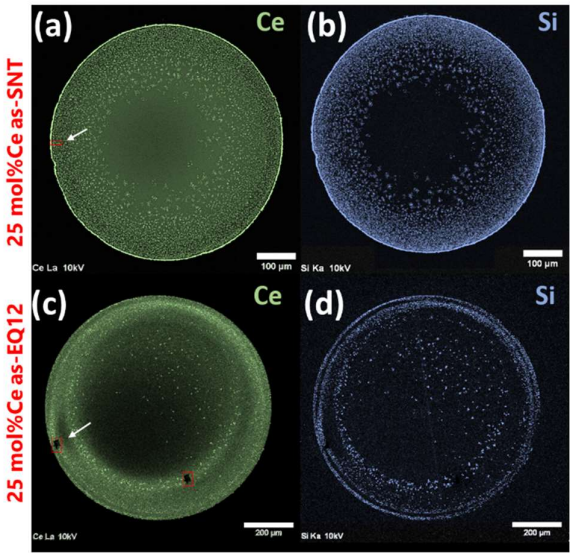

Figure 3: EPMA Ce and Si elemental maps obtained on cross-sections of an as-sintered and an as-equilibrated particle respectively, both having $\chi(Ce)_{analyzed}$= 25 mol% Ce. White arrows indicate the extraction location of FIB lamellae investigated by TEM.

This observation pointed to the existence of another crystallographic phase that was not recognized in the first series of X-ray diffractograms. A new XRD measurement campaign with an increased acquisition time and a significantly larger sample quantity in order to improve the detection of traces of a non-fcc phase in the patterns was executed. The results of the as-sintered IGMS are summarized in Figure 4 and reveal the existence of an additional phase, which was identified as Ce-oxyapatite, $Ce_{4.67}(SiO_4)_3O$ (#PDF2: 00-043-0441,[33]). The reflections at angles of 28.21° (42 %), 30.92° (100 %), 31.19° (53 %) and 47.89° (38 %) were used to determine the presence of this phase in the composition, and the percentages listed in parentheses correspond to their respective intensity ratios (I/I_0). The phase has a Ce content of ≈ 60 mol% and an O/*M* ratio of ≈ 1.7, which is consistent with what is recurrently observed for Ce-rich precipitates by the EPMA maps in the zones of interest. The cut-outs of the diffractograms on the right-hand side of Figure 4 show the square roots of the normalized intensities to highlight the traces of the Ce-Si-O phase.

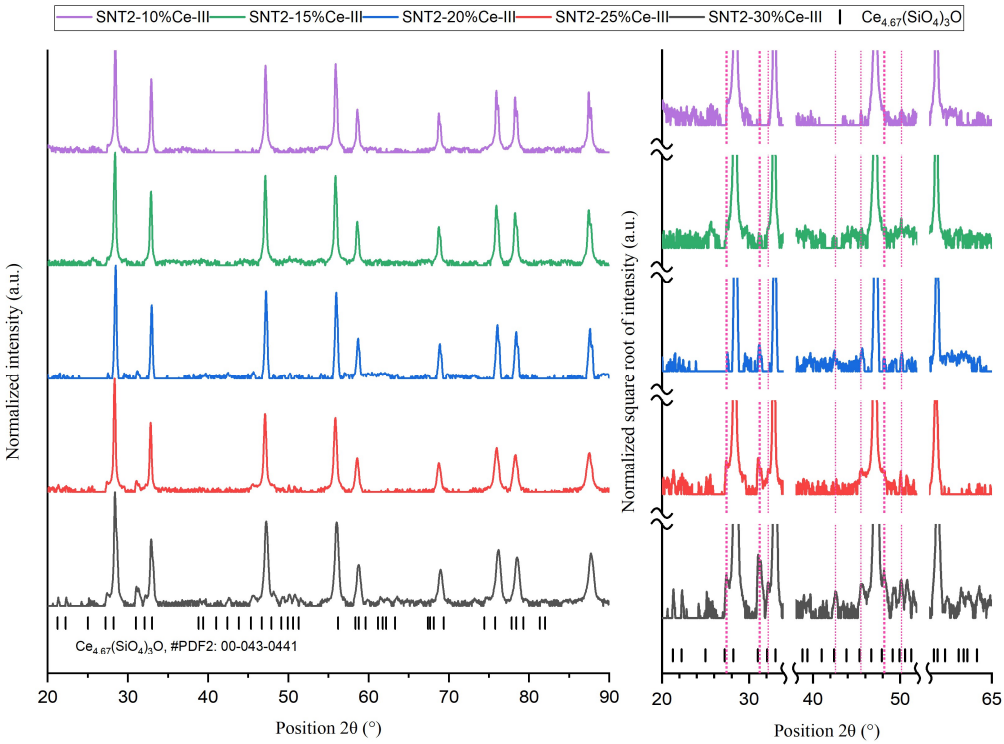

Figure 4: X-ray diffractograms taken on as-sintered ground IGMS with χ(Ce)={10 mol%, 15 mol %, 20 mol %, 25 mol % and 30 mol%} with acquisition and sampling optimized for the detection of the Ce-oxyapatite trace phase. Left: Comparison of normalized intensities of the full patterns between 20° and 90° 2θ. Right: Square root of normalized intensity of pattern cut-outs to better visualize the peaks belonging to the trace phase(#PDF2: 00-043-0441,[33]*). High-intensity lines which exhibit cut-off peak-tops belong to the fcc pattern.*

To study the microstructural nature of the trace phase with a higher resolution than achievable by EPMA, lamellae were extracted by FIB for TEM analysis. Regions with high occurrence of Si-Ce enriched features were selected, as indicated by the arrows in Figure 3. EDS maps of these lamellae (Figure 5) show grains containing (I) Ce and Si, but no U, as well as grains containing (II) U and Ce, but no Si. This is a strong evidence for a negligible solubility of Si in the $(U,Ce)O_{2\pm x}$ matrix of the fcc phase. It most likely segregates during the formation of the solid solution. Quantitative point measurements on the Ce-Si-O grains showed that the Si content and Si/Ce ratio in these EDS mappings are found to be very close between the as-sintered and as-equilibrated states. The results are consistent within and between the various FIB lamellae. Electron diffraction patterns obtained on various Ce-Si-O grains match well to the phases identified via XRD. For example, when oriented along the [010] zone axis the diffraction patterns of Figure 5f (space group P63/m, a=9.6578 Å, c=7.1187 Å) are in excellent agreement with the hexagonal lattice of $Ce_{4.67}(SiO_4)_3O$. Practically identical findings were made on a lamella taken from one of the inner precipitate rings of an as-equilibrated particle (Figure 5g-l).

The Ce content of the directly neighboring, Uranium-rich, grains is significantly lower than what would be expected based on the quantitative EPMA line scan (Figure 2 b). The relative Ce local depletion is directly proportional to the neighboring presence of Si. This points to a pronounced case of selective scavenging of Ce by $Si(O_x)$ to form the non-fcc $Ce_{4.67}(SiO_4)_3O$ phase in the immediate surrounding of the latter grains, under the thermodynamic conditions applied. The latter favor the formation of $Ce_{4.67}(SiO_4)_3O$ over the other two possible $nCe_2O_3{\cdot}mSiO_2$ phases, as reported in literature[34]. It should be noted that the FIB extraction areas presented in Figure 5 are located at the outer rim where a high Si contamination is observed, presenting therefore a higher amount of Ce-Si-O phase and surrounding Ce depletion than in the bulk.

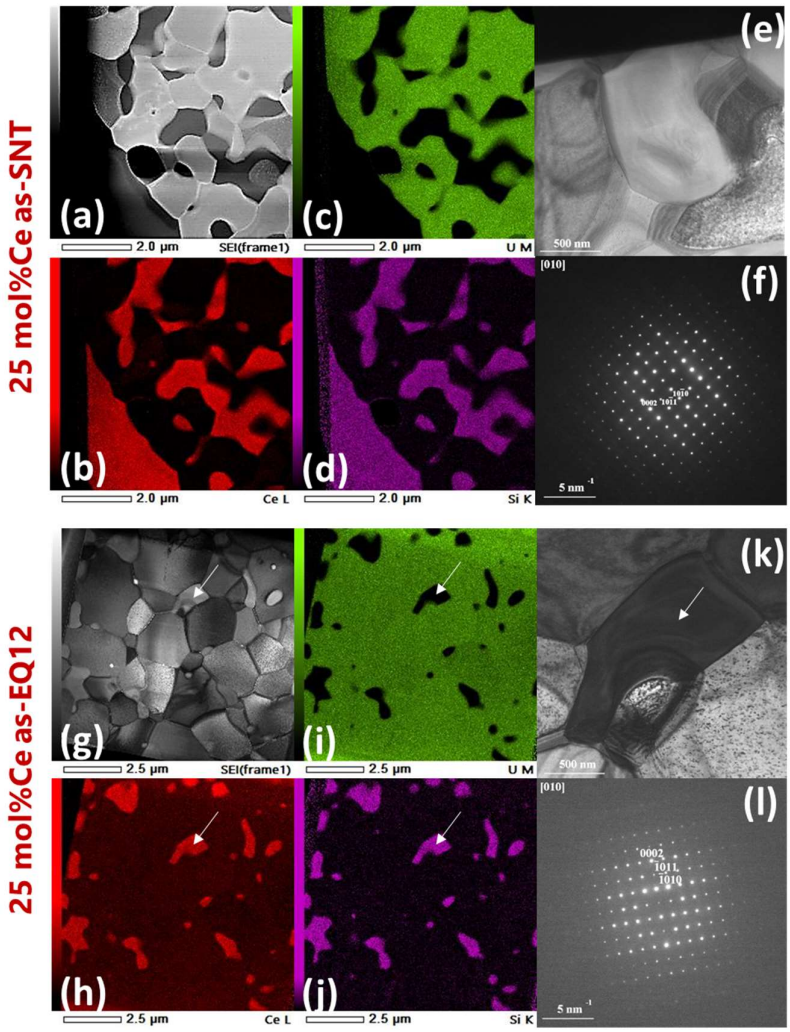

Figure 5: STEM-EDS study of two FIB lamellae extracted from χ(Ce)=25 mol% samples in; ***Top row****: as-sintered (SNT) state, showing a) the STEM image, b) Ce-, c) U-, d) Si-maps, as well as e) bright field image and f) diffraction pattern of a* $Ce_{4.67}(SiO_4)_3O$ *particle; and* ***Bottom row****: as-equilibrated (EQ-12) state, showing g) the STEM image, h) Ce-,i) U-, j) Si-maps, as well as k) bright field image and l) diffraction pattern of a* $Ce_{4.67}(SiO_4)_3O$ *particle.*

Lastly, both the more general overview of the EPMA Ce-map as well as the TEM results on the FIB lamellae show a notable decrease in number density and size of the Ce-Si-O precipitates going from the as-sintered to the as-equilibrated state. This observation on both scales gives strong indication for cation mobility during the equilibration treatment, despite the rather low treatment temperature of 1073 K. Although this does not seem to affect the average composition and global O/*M* ratios of the fcc bulk, it does seem to have an observable effect on the spatial U/Ce and Si distribution.

4. Discussion

In order to help explaining, and potentially fit, the asymmetrical/split XRD peak shapes, an indirect quantification of the Ce distribution within IGMS was attempted using EPMA quantitative radial line scans. Local Ce enrichment was probed every micrometer from the center to the particle edge along a given radius (Figure 6a and Figure 6c). The shape of the χ(Ce) distribution in the line scans along the particles' radius confirms the qualitative observations made from the elemental cation distribution

mapping of the entire cross-section in Figure 1 and Figure 2. It depicts a combination of a radially varying Ce background level, increasing towards the rim (r/R=1) of the particle with two maxima at the periphery and local Ce spikes (for χ(Ce)≥15 mol%) related to the Ce-Si-O precipitate phase which were randomly present on the line scan path.

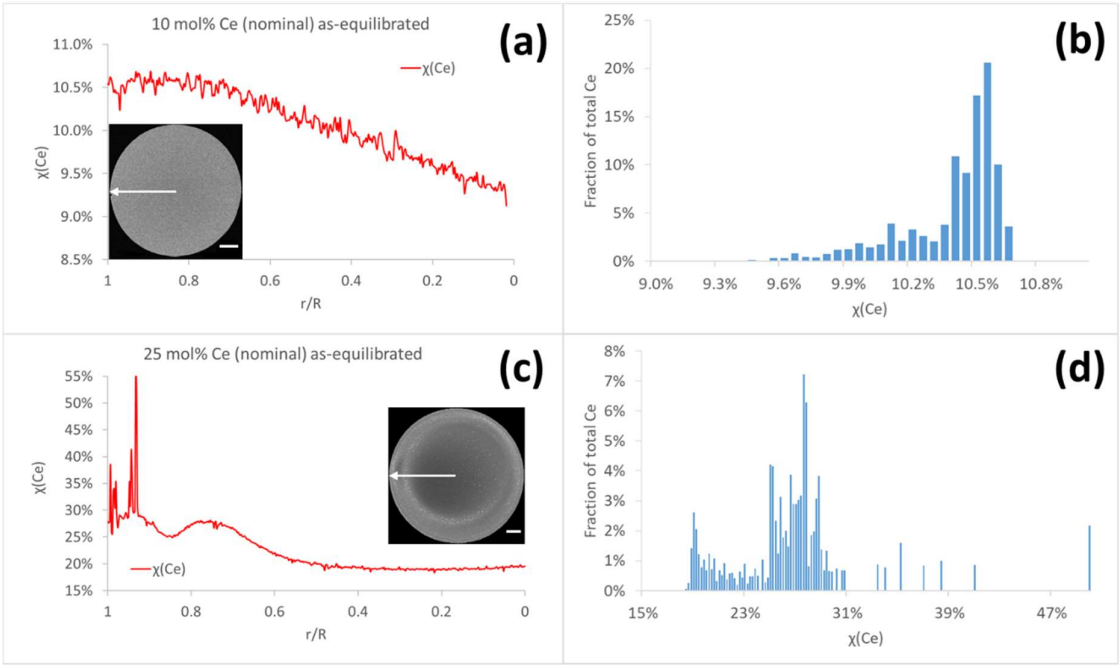

Figure 6: Results of EPMA radial line scans (left) of polished cross-sections of IGMS with Ce contents of 10 mol% (a) and 25 mol% (c), as well as histograms of the Ce distribution (right) in the IGMS with Ce contents of 10 mol% (b) and 25 mol% (d). Scale bars on EPMA maps indicate 100 µm.

To obtain a rough estimate of the distribution of the Ce fractions in terms of χ(Ce) frequency in the particles from quantitative EPMA line scans, the quantitative point measurements, with roughly a 1 µm³ interaction volume, were weighted in function of their position along the radius of an assumed perfect sphere. This geometric weighing was necessary due to the r^3-dependent contribution of each radial measurement point to the total Ce distribution histogram. The resulting histograms are shown as Figure 6b and 6d for the particles with Ce contents of 10 mol% and 25 mol%, respectively. For the 25 mol% Ce batch, the Ce distribution shows a main maximum between 25 mol% and 30 mol% Ce and a minor around 18 mol% Ce. Location of maxima is quite dependent on the specific radius selected for the line scan since variations in the concentric Ce distribution varies somewhat within a particle, but the bimodal distribution was repeatedly found on all other line scans performed in several particles. The local Ce-rich spots with χ(Ce) > 50 mol% so far have been observed to consist only of the Ce-Si-O phase. Ce-rich spots with χ(Ce) > 50 mol% (Ce-Si-O phase) do not seem to substantially influence the Ce distribution in the fcc matrix. The bimodal nature of the distribution is even clearer for the 30 mol% Ce microspheres where the two distribution peaks are more evenly distributed. On the other hand, a unimodal slightly left-skewed distribution is observed for χ(Ce) = 10 mol%, which is too narrow to be reflected in the peak shapes of corresponding XRD pattern. The significant deviation from a sharp-Gaussian distribution of Ce shown in the extrapolated quantitative line scan is consistent with XRD peak shapes that exhibit near-splitting from 25 mol% Ce onwards and an asymmetric skewed and broadened shape below 25 mol% Ce.

It should be noted that the presence of $Ce_{4.67}(SiO_4)_3O$ is monotonously increasing with increasing Ce content, as shown in Figure 4. The mass fraction of this phase is seen to increase with local Ce and Si

availability such that no particularly evident macroscopic lower threshold for the presence of either could be determined. Therefore, although it was not detected in this work, the trace presence of the Ce-Si-O phase can also not be categorically ruled out below a global composition of 10 mol% Ce.

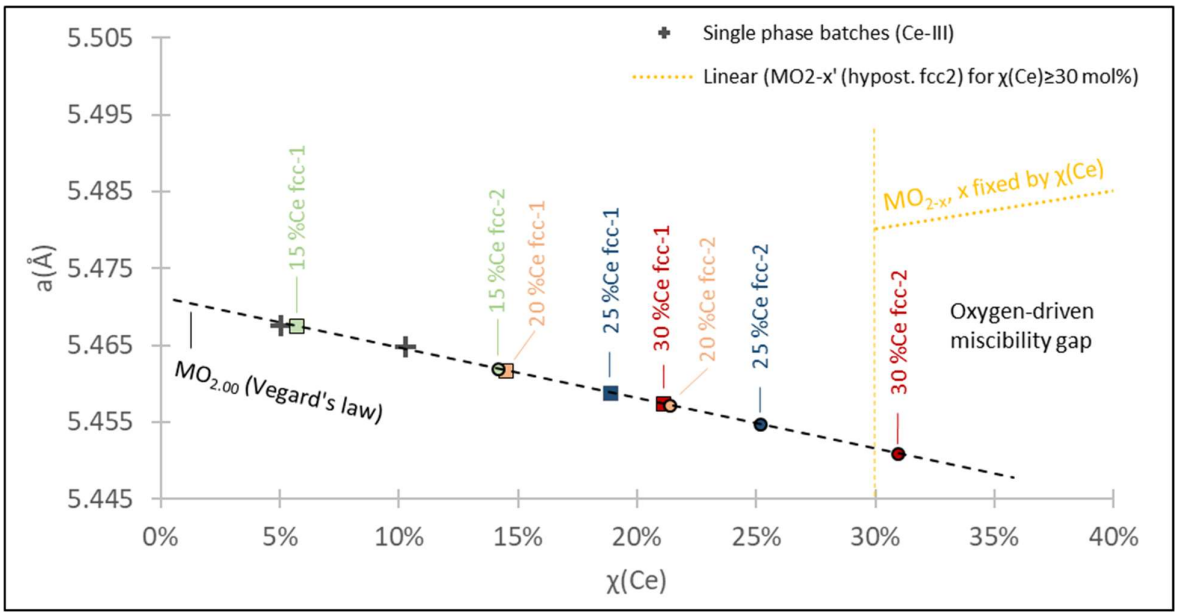

Figure 7: Results, given as LP_{fcc} in function of $\chi(Ce)_{fcc}$, of the phase quantification effort using a three-phase refinement model representing the underlying quasi-bimodal Ce distribution for non-monophasic compositions via two-fcc model-phases. The excess χ(Ce) is assigned to the non-fcc $Ce_{4.67}(SiO_4)_3O$ phase. Each composition that was fitted via the bi-modal model, $\chi(Ce)_{nominal}$={15 mol%, 20 mol%, 25 mol%, 30 mol%}, is depicted with ● ● ● ● in the given order representing the U-rich fcc1 and, with ■ ■ ■ ■ Ce-rich fcc2 model phases respectively.

The bi-modal character of the total Ce mass distribution in function of χ(Ce) was observed to be systematic in data obtained by radial EPMA quantitative line scans on particle batch whose XRD pattern showed asymmetric XRD peak broadening and peak splitting. Therefore, a simplified model consisting of two stoichiometric fcc phases (U-'rich' fcc1 and Ce-'rich' fcc2) and the hexagonal Ce-Si-O trace phase was proposed to fit the XRD data by a Rietveld refinement. When a two-fcc-phase Rietveld fit is executed, the sum of the obtained χ(Ce) values resulted in some residual Ce to be accounted for. This residual Ce was assigned to the third non-fcc $Ce_{4.67}(SiO_4)_3O$ phase as a first estimate. The corresponding Ce content in the $Ce_{4.67}(SiO_4)_3O$ phase was subtracted from $\chi(Ce)_{analyzed}$ (obtained via ICPMS) for each composition. The remaining $\chi(Ce)_{fcc}$ was then distributed among the two fcc model phases. The LPs obtained can directly be translated into χ(Ce) values through the Vegard's law when non-stoichiometry of the fcc phase(s) is excluded, the plausibility of which will be explained further. The LP obtained from fcc1, by fitting the lower angle side of XRD peaks, was used to obtain a corresponding χ(Ce) by assuming validity of the Vegard's law. The remaining Ce was assigned to the fcc2 phase. As illustrated in Figure 7, the resulting LP of the fcc2 phase was then seen to fall in line with the Vegard's law. If the $Ce_{4.67}(SiO_4)_3O$ phase is ignored in the refinement model, a systematic excess of unaccounted Ce for the Ce-rich fcc2 phase is obtained, similar to the interpretation in [24], leading to a significant deviation of the fcc2 phases' LP from Vegard's law. This had to be excluded as significant hypo-stoichiometry was shown to be implausible in this work. Indeed, the presence of a hypo-stoichiometric fcc $MO_{2-x'}$ phase, known to co-exist at room temperature with a stoichiometric $MO_{2.00}$ phase due to a miscibility gap for the χ(Ce) ≥ 30 mol% domain can be excluded with certainty based on the XRD patterns alone. This is because the reported fcc lattice parameters [17], [25] of the former would be found in a domain that is significantly above the range that could be obtained from the given XRD patterns (see yellow dotted

line in Figure 7). On the other hand, reflections of a hypothetical MO_{2-x} generated by the χ(Ce) < 30 mol% values are not observed either or their intensity is so small that they are masked by the broad convolution of the $MO_{2.00}$ peaks, in which case the mass fraction of MO_{2-x} would be strictly constrained to insignificance. When the Rietveld refinement is repeated with this third phase, and given the fixed Ce-content in the $Ce_{4.67}(SiO_4)_3O$ phase, the wt.% values obtained for this third trace phase in each composition were seen to roughly match the χ(Ce) that was accounted for by the a priori estimation. In summary, although considerable simplifications were made, this model lead to a good refinement of the XRD data while respecting stoichiometry. The systematic U/Ce cation distribution heterogeneity patterns, and the presence of the hexagonal Ce-Si-O trace phase representing the highly Ce-enriched precipitates, that this study uncovered, explain the entirety of the deviations from single phase fcc behavior observed in the XRD patterns.

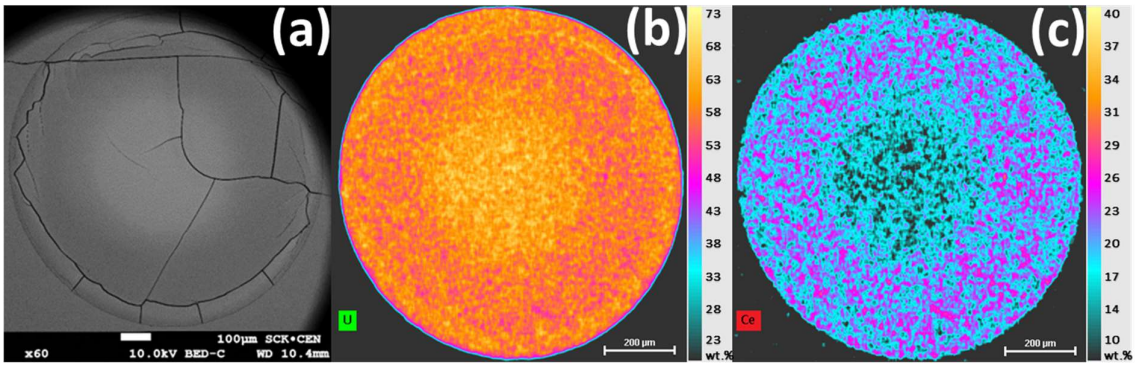

Figure 8: (a)BSE image of a cross-section of an as-dried IGMS with χ(Ce) = 25 mol%, its EDS mapping results in wt.% for U(b) and Ce(c) respectively.

IGMS cross-sections of the *as-dried* states were examined in order to understand the origin and evolution of the U/Ce cation distribution heterogeneity and Si contamination. The particles in the *as-dried* state consist mainly of ammonium diuranate (ADU, $3UO_3{\cdot}2NH_3{\cdot}4H_2O$) for the U-precursor[35], and a Ce-precipitate likely incorporated into the ADU matrix [36], as well as some possible residual moisture and traces of gelation agents. The chemical form in which Ce is incorporated into the microsphere is currently not known as no distinct XRD pattern, e.g. for $Ce(OH)_3$, or $Ce(OH)_4$ could be identified in a recent study [36]. This is in contrast to calcined and sintered mixed oxides, that are, depending on the subjected heat treatment, already (partially) densified into a solid solution. Preparing a cross-section of an as-dried particle was found to be challenging due to this material being essentially a soft gel bead. Furthermore, the cross-sections of materials in this state were particularly beam sensitive, making it impossible to conduct EPMA studies, while, due to the much lower beam current, SEM/EDS investigations were possible. Figure 8 shows the (a) BSE image of the cross-section of an *as-dried* IGMS with χ(Ce) = 25 mol%, (b) U, and (c) Ce elemental mapping via EDS. The latter two show an enrichment of U and a Ce depletion at the center of the particle, evidencing elemental segregation in the gelated state and thus prior to any thermal treatment. Moreover, the presence of Si in the *as-dried* microsphere was detected but no definitive statement can be made on its origin in this study because of the very low amount, the sample beam sensitivity and possible cross-contamination of the soft and porous surface of its cross-section during sample preparation.

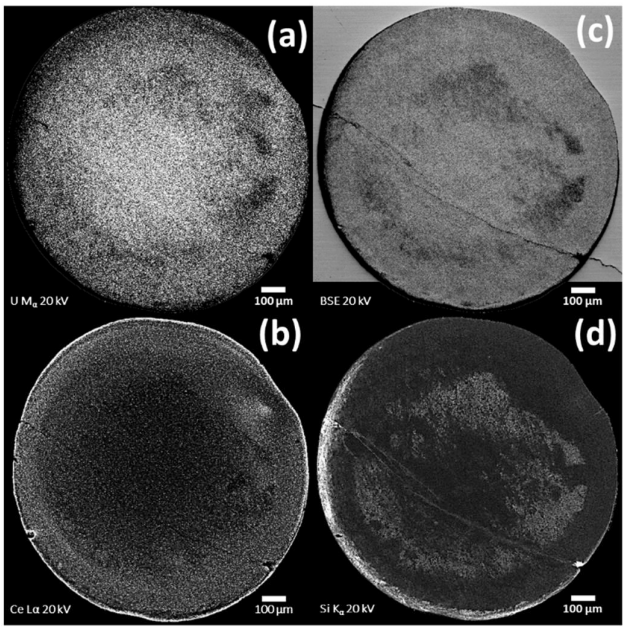

Figure 9: Elemental mapping results of an as-pre-sintered IGMS with χ(Ce)= 25 mol% for (a)U, (b)Ce, (d)Si and its (d)BSE image taken on the cross-section of an as-pre-sintered particle of the same composition obtained via EPMA.

The subsequent state to the *as-dried* one is the *as-calcined* state, which is achieved by calcination, and in which microspheres consist of extremely porous and weakly bonded spheroidal powder agglomerates of mixed oxides of U and Ce at or close to their highest oxidations states, U_3O_8 and CeO_2 respectively, as confirmed by XRD measurements. Due to the relatively low temperature of 1173 K, the short duration (1 h) as well as the phases they represent, the mechanical strength of the as-calcined state is so low that particles are dispersed upon contact with handling tools. Hence, it was ruled to be impractically challenging to prepare particles ceramographically in this state. To investigate nevertheless the cation distribution at a stage as close as possible to the as-calcined one, a very short sintering at a relatively low temperature of 1473 K for 1 h, under an $\mu(O_2)$ = -420 kJ/mol for comparability with the main series, was executed on *as-calcined* particles with 25 mol% Ce. This *pre-sintered* state offered just enough mechanical stability for ceramographic preparation by barely inducing necking between the constituent powder particles. This made sure that the original cation distribution heterogeneity patterns of the *as-calcined* state were preserved to an overwhelming extent.

One of the studied cross-sections of a pre-sintered IGMS with χ(Ce)=25 mol% is depicted in Figure 9, where the U, Ce and Si elemental mappings obtained via EPMA are shown in (a), (b) and (d) respectively, while (c) shows the corresponding BSE image. Multiple observations were made on the cross-section of the as-pre-sintered state: The U-rich and Ce-rich regions are inversely correlated, as seen before in the as-sintered and as-equilibrated states, and are found in the center and annular periphery respectively, with a particularly Ce-enriched thin “crust” located at the outermost boundary of the particle. Furthermore, there is a moderately Si-enriched region of irregular shape located between the U-rich center and Ce-rich annular regions without visible correlation with U or Ce, and finally, a highly Si-enriched crust coinciding with some portions of the Ce-rich crust. The outer crust section located on the bottom-left quadrant at which the width of the Si-crust is larger, is seen to be also almost devoid of U. The observations on these regions are supported by the corresponding BSE image, where the U-rich center region of the cross-section is shown as a high-Z contrast region. The Ce-rich annular region, the locations corresponding to the shape of the Si-rich intermediate region, as

well as the partial Ce-Si enriched outer crust segment are shown with significantly lower Z-contrast. Finally, quantitative EDS measurements, not shown here, provide unmistakable evidence for the authenticity of the Si presence.

In summary, the following statements on the elemental distribution at different stages of the microsphere preparation as shown in Figure 8, Figure 9 and in other similar cross-sections not shown here, can be made:

1. A significant U/Ce spatial distribution heterogeneity is present already in the *as-dried* state and persists in the *pre-sintered* state. The cause of this initial heterogeneity is currently not known and its investigation was not within the scope of this work.
2. Si presence is evidenced unambiguously at the pre-sintered state. Si within the bulk of the particles is an indication that the contamination very likely predates the post-drying thermal treatments.
3. It was not possible to unambiguously conclude on the presence of Si in the dried state due to experimental limitations while it cannot be excluded either due to the non-negligible presence above the background signal in numerous acquired EDS spectra.

At the time- and space-dependent microscale, while detailed studies exist for the internal gelation of pure Uranyl Nitrate[37], [38], the co-gelation of the U and Ce is a complex process that is not yet exhaustively described in literature so far. It involves various chemical steps that happen in rapid succession [37], [38]. Investigating and understanding in detail the gelation process is a challenging task as it can be influenced by multiple factors happening at very small scales such as the mixing of reactants, the droplet formation, the displacement and likely start of surface interaction upon contact with the Si-oil, and finally by the heat propagation from the hot gelation medium into the broth droplet triggering HMTA and Urea protonation/decomposition[37]. This leads to a release of ammonia causing the subsequent precipitation of UO^{2+} and Ce^{3+}/Ce^{4+} species[39], [40]. For each species, precipitation may progress on separate paths with different reported pH ranges[39] and kinetics while resulting in different products[39], [41]. While the exact chemical form of the Ce-rich precipitate currently is not known [24], [37], [39], the progress and products of the former is reported to depend on temperature and R factors for HMTA and Urea as well as metal concentrations. It likely also depends on local variations of pH in time [1], [3], [5]. It should be noted however that the data on co-precipitation UO^{2+} and Ce^{3+}, as cited in[39], has been collected only in decomposing urea. The authors are not aware of a full-scoped study that includes U, Ce, Urea and HMTA while studying time-dependent local interactions. If indeed two or more distinct precipitate species and/or gradients of cation incorporation into the these phases result during gelation post-gelation, it will be passed along the subsequent treatment steps. The step during which the HMTA/Urea decomposition and the precipitation reaction is ongoing together with the sinking of the droplet involves the largest matter conversion and movement. Thus the authorship considers these two overlapping steps as having the highest potential contribution to cation heterogeneity. Nevertheless, in a future study, it is advisable to also investigate the role of premature gelation as well as the aging step as a potential contributor to the heterogeneity phenomena described in this study. Ultimately, the exhaustive description of these possible effects alone would be far outside the scope of this work and would require a separate study.

The initially rather diffuse Si presence prior sintering clearly condenses during sintering into the distinct crystalline Ce-Si-O precipitates. Si can be expected to diffuse during densification towards free surfaces and bound with Ce in the trivalent state. The abundant presence of the trivalent state at temperatures at or above 1273 K, which is commonly applied during reductive sintering, is a precondition to the formation of this oxyapatite phase. Once formed, and practically all available Si is consumed, $Ce_{4.67}(SiO_4)_3O$ is thermodynamically stable over a large temperature range as long as the conditions remain reductive or inert at the given treatment temperature profile [42]–[44]. This observation is

likely to be of critical concern of other An/*Ln* systems that possess cations which either can only be in the trivalent state or have significant fractions of their multivalence state in the trivalent state when in a mixed oxide solid solution. Indeed, towards the final phases of the present work, the reported presence of highly Nd-enriched features in Nd-infiltrated IGMS [45] have been also identified as Nd-oxyapatite in unpublished work of Çolak et al.. Furthermore, Uygur et al. also revealed, in unpublished work, varying presence of the Ce-oxyapatite in (U,*Ce*)$O_{2\pm x}$ materials synthesized not only via IG but also via other mixed oxide synthesis routes. For pure $UO_{2\pm x}$ this had not been observed so far. This is due to the fact that U has no 3+ state in dioxide form, thus has not been observed to form an analogue to the *Ln*-oxyapatite or related phases. Due to the difficulties of detecting trace amounts of Si, it is possible that, when present, it has been often overlooked, or possibly even misinterpreted as *Ln*-'micro-segregation' as briefly touched upon in [46]. The wider availability of appropriate techniques is expected to lead to more frequent detection of analogous *An/Ln*-silicate trace phases, or to definitive evidence for the lack of thereof, in future work.

These consequences for the sintered microstructure of the particles brought upon by a very small amount of Si contamination makes the search for its origin as well its avoidance paramount. Although an experimental investigation is not within the scope of this work, some condensed hypothetical considerations shall be advanced. The authors currently suspect two, possibly independent, Si sources: (I) Contamination of the gelated microspheres by Si-oil residues; (II) Surface deposition of Si-species volatilized from SiO_2 in the furnace environment. For path (I) traces of PDMS might have persisted despite the washing procedure in petroleum benzine as described in[24]. Contamination via this path could also involve the hypothetical depolymerization products of PDMS, which are formed at prolonged contact in high pH environments, most of which are water soluble, i.e. dimethylsilanediol (DMSD) [47], [48]. High pH values occur at various stages of the IGMS fabrication process, i.e. gelation and aging in ammonia solution. Water soluble decomposition products would in part also diffuse into gelated IGMS. However, an initial estimation using the reported values reported in [49]yields that the kinetics of this path might still be too slow to account for the Si presence observed in this study. (II) Surface deposition of Si-species volatilized from SiO_2 in the furnace environment during high-temperature heat treatments in a low oxygen partial pressure atmosphere, e.g. SiO, SiH_4 or $Si(OH)_4$, could either occur from refractory insulation [50] material, or it could be a secondary cross-contamination from SiO_2 formed from the calcination of the Si-oil residues. Since Si-oil is widely used for internal gelation work, it might be of future interest to obtain an experimentally backed conclusion, which was however outside the scope of this study.

Organochlorines, i.e. carbon tetrachloride [15] and trichloroethylene[51]–[53] were often reported as washing agents to remove the gelated particles of Si-oil. Since no study on Si trace presence nor a systematic study on cation distribution homogeneity is known, it cannot be stated whether the use of either was particularly advantageous in regard to the absence of unwanted cation distribution features and/or on the absence of Si residues in the final product. Even in case this is demonstrated to be true, organochlorines need to be also evaluated in light of their environmental and health-related risks and in particular concerning their property as mixed radioactive secondary waste when deployed in larger quantities. Alternative gelation media, e.g. carbon tetrachloride[13] or 2-ethyl-1-hexanol[3], and/or alternative washing agents, e.g. NuSolv SOR-C, as suggested in [54], or use of oil-free gelation approaches like microwave heating [55]–[57] would need to be studied further.

5. Conclusion

The main aim of this study was to understand the peak shape anomalies observed at high 2θ angles in the XRD patterns of sintered and equilibrated (U,Ce)O_2 IGMS. The first hypothesis, a phase separation based on oxygen stoichiometry was probed via TG. As the obtained results were contradictory to the

expectations, a departure from single phase behavior due to cation distribution heterogeneity was investigated. The results clearly showed that in the as-sintered state, as well as in the as-equilibrated state, the IGMS showed systematically increasing U/Ce distribution heterogeneity with increasing nominal χ(Ce). Internally gelated mixed *An*/*Ln* oxide microspheres so far are generally reported on the basis of their XRD patterns, or assumed[3] to possess cation homogeneity. However, this work has shown that for a currently unknown domain of process parameter combinations this might not be valid at the microscale. Although these findings do not allow a categorical generalization, they have nevertheless a more general significance since the used parameters and conditions fell within the domain of commonly applied gelation parameters, temperature regime, washing procedure and other process conditions to obtain (*An*/*Ln*)O_2 microspheres.

The origin of the heterogeneities was traced back throughout the fabrication steps up until the as-dried state and observed to evolve from a rather diffuse characteristic into more refined and contrasted structures during calcination and sintering/equilibration, respectively. The initial Ce-heterogeneity patterns that were observed already in the as-dried state are suspected to be formed during gelation and to have evolved into its final state during thermal treatment. The Ce-rich precipitates were unambiguously characterized to consist of the hexagonal P63/m $Ce_{4.67}(SiO_4)_3O$ phase. Long segments of the thermal treatment history were seen to coincide with the well-reported domain of thermodynamic formation conditions of the apatite phase. The unexpected Si presence and the formation of the non-fcc Ce-Si-O trace phase as single grain $Ce_{4.67}(SiO_4)_3O$ precipitates, and local clusters thereof, have been shown to be responsible for capturing non-trivial amounts of Ce from the surrounding fcc (U,Ce)O_2 matrix grains. On a global scale, this was seen to be of significance in attempting to semi-quantitatively explain the relation between fcc XRD patterns and the Ce-distribution throughout the IGMS.

The relative depletion of local Ce in the U-rich center of the particles observed prior heat treatments, combined with the incompatibility of Si species in fcc (U,Ce)$O_{2\pm x}$, its affinity with Ce^{3+} and the volatility of SiO and other Si-species during sintering in reducing atmospheres, will all contribute to the final microstructure observed. The investigation of the causes and factors leading to cation distribution heterogeneity in the as-dried particles would require a dedicated study of the very likely contribution acquired throughout the chemical phase of the particles, i.e. gelation, washing and ageing. It is reasonable to hypothesize that the most likely fabrication step where the macroscopic aspects of the asymmetry was introduced has been during the simultaneously happening steps, precipitation and sinking along the gelation medium, where thin liquid film hydrodynamics potentially act together with the complex physical chemistry going on during gelation.

Due to the critical effect the trace presence of Si was shown to have on the microstructure of (U,Ce)O_2 IGMS, possible Si contamination sources should be avoided. Alternatives to the Si oil, and/or washing agents as well as oil-free fabrication may also be considered. The microwave gelation offers such a process, which in addition allows to omit the laborious washing, which also results in radioactively contaminated liquid waste. Other possible Si cross-contamination from glassware or deposition occurring during thermal treatments (calcination and/or sintering furnace) must be regularly checked and avoided. Many studies working with internal gelation have assumed, e.g. [58], categorical homogeneity for (U,*Ln*)O_2 IGMS systems but a deviation from a perfect solid solution seems to be possible under a combination of process parameters which were not within the scope of this work. Furthermore such deviations can easily be missed without a careful analysis of the XRD pattern at high 2θ angles and the type of detailed internal elemental distribution analysis presented in this work. Further work may be required to study more systematically the sensitivity of internal gelation to the

variation of synthesis parameters, trace contaminants and precursor chemicals in regard to cation homogeneity in the final product.

6. Declaration of competing interest

The authors are not aware of any competing material interest or other relationships that could have impacted scientific impartiality of this study.

7. CRediT authorship contribution statement

Selim Uygur: Conceptualization, Methodology, Writing - original draft, Validation, Formal analysis, Investigation, Data curation, Visualization. **Rémi Delville**: Methodology, *Writing - original draft*, Writing - review & editing, Validation, Data curation, visualization, Supervision, Project administration, Resources. **Christian Schreinemachers**: Investigation, Writing - review & editing, Validation. **Gregory Leinders**: Methodology, *Writing - original draft*, Writing - review & editing, Validation, Formal analysis, Supervision, Project administration. **Nico Vanhove**: Investigation, Writing - review & editing. **Wouter van Renterghem**: Investigation, Formal analysis, Writing - review & editing. **Jozef Vleugels:** Writing - review & editing, Supervision. **Marc Verwerft**: Writing - review & editing, Supervision, Project administration, Resources.

8. Acknowledgements

The authors acknowledge financial support of this research provided through the SCK CEN Academy for Nuclear Science and Technology (Belgium), the MYRRHA project (SCK CEN, Belgium) as well as funding provided through the Energy Transition Fund of the Belgian FPS Economy within the framework of the ASOF – Advanced Separation for Optimal management of Spent Fuel) project. The authors express recognition of technical staff of SCK•CEN, in particular Peter Dries, Koen Vanaken (†), Kris Kaers and Jelle Van Eyken, for continued technical and logistical support during this study.

9. References

[1] P. Naefe and E. Zimmer, “Preparation of Uranium Kernels by an External Gelation Process,” *Nucl Technol*, vol. 42, no. 2, pp. 163–171, Feb. 1979, doi: 10.13182/NT79-A32147.

[2] G. Ledergerber, “Internal Gelation for Oxide and Nitride Particles,” 1996.

[3] Jeffrey A. Katalenich, “Production of Monodisperse, Crack-Free Cerium Oxide Microspheres by Internal Gelation Sol-Gel Methods,” 2014.

[4] J. B. W. Kanij, A. J. Noothout, and O. Votocek, “The KEMA U(VI)-process for the production of UO_2 microspheres.” 1974. Accessed: May 11, 2023. [Online]. Available: https://inis.iaea.org/search/search.aspx?orig_q=RN:5132968

[5] C. Ganguly, U. Linke, and E. Kaiser, “Characterization of (U,Ce)O_2 pellets prepared by the sol-gel microsphere pelletization process,” *Metallography*, vol. 20, no. 1, pp. 1–14, 1987, doi: 10.1016/0026-0800(87)90061-9.

[6] M. A. Pouchon, G. Ledergerber, F. Ingold, and K. Bakker, “Sphere-Pac and VIPAC Fuel,” in *Comprehensive Nuclear Materials*, Elsevier, 2012, pp. 275–312. doi: 10.1016/B978-0-08-056033-5.00059-8.

[7] J. F. Vigier, K. Popa, V. Tyrpekl, S. Gardeur, D. Freis, and J. Somers, “Interaction study between MOX fuel and eutectic lead-bismuth coolant,” *Journal of Nuclear Materials*, vol. 467, pp. 840–847, 2015, doi: 10.1016/j.jnucmat.2015.10.056.

[8] S. Suryanarayana, N. Kumar, Y. R. Bamankar, V. N. Vaidya, and D. D. Sood, “Fabrication of UO_2 pellets by gel pelletization technique without addition of carbon as pore former,” *Journal of Nuclear Materials*, vol. 230, no. 2, pp. 140–147, Jun. 1996, doi: 10.1016/0022-3115(96)00162-6.

[9] H. Daniels, S. Neumeier, A. A. Bukaemskiy, G. Modolo, and D. Bosbach, "Fabrication of oxidic uranium-neodymium microspheres by internal gelation," *Progress in Nuclear Energy*, vol. 57, pp. 106–110, May 2012, doi: 10.1016/j.pnucene.2011.12.016.

[10] C. Schreinemachers, A. A. Bukaemskiy, M. Klinkenberg, S. Neumeier, G. Modolo, and D. Bosbach, "Characterization of uranium neodymium oxide microspheres synthesized by internal gelation," *Progress in Nuclear Energy*, vol. 72, pp. 17–21, 2014, doi: 10.1016/j.pnucene.2013.07.016.

[11] K. S. Kumar, T. Mathews, H. P. Nawada, and N. P. Bhat, "Oxidation behaviour of uranium in the internally gelated urania-ceria solid solutions - XRD and XPS studies," *Journal of Nuclear Materials*, vol. 324, no. 2–3, pp. 177–182, 2004, doi: 10.1016/j.jnucmat.2003.09.014.

[12] G. Gündüz, I. Önal, and H. H. Durmazuçar, "Pore size distributions in uranium dioxide and uranium dioxide-gadolinium oxide fuel kernel produced by sol-gel technique," *Journal of Nuclear Materials*, vol. 178, no. 2–3, pp. 212–216, 1991, doi: 10.1016/0022-3115(91)90388-N.

[13] S. Yamagishi and Y. Takahashi, "Production of $(Th,U)O_2$ Microspheres with Uranium Content of 0–35% by Sol-Gel Process Using CCl_4 as Gelation Media," *J Nucl Sci Technol*, vol. 23, no. 9, pp. 794–801, Sep. 1986, doi: 10.1080/18811248.1986.9735056.

[14] F. Ingold, J. Wichser, R. Zubler, M. Street, Z. Kopajtic, and S. Kono, "Fabrication of neptunium containing MOX fuel microspheres," *J Nucl Sci Technol*, vol. 39, no. sup3, pp. 717–720, Nov. 2002, doi: 10.1080/00223131.2002.10875567.

[15] A. Kumar *et al.*, "Studies on preparation of $(U_{0.47},Pu_{0.53})O_2$ microspheres by internal gelation process," *Journal of Nuclear Materials*, vol. 434, no. 1–3, pp. 162–169, 2013, doi: 10.1016/j.jnucmat.2012.11.009.

[16] R. D. Shannon, "Revised effective ionic radii and systematic studies of interatomic distances in halides and chalcogenides," *Acta Crystallographica Section A*, vol. 32, no. 5, pp. 751–767, 1976, doi: 10.1107/S0567739476001551.

[17] T. L. Markin and R. S. Street, "The uranium-cerium-oxygen ternary phase diagram," *Journal of Inorganic and Nuclear Chemistry*, vol. 32, pp. 59–77, 1970, doi: https://doi.org/10.1016/0022-1902(70)80449-3.

[18] D. I. R. Norris and P. Kay, "Oxygen potential and lattice parameter measurements in $(U,Ce)O_{2-x}$," *Journal of Nuclear Materials*, vol. 116, no. 2–3, pp. 184–194, 1983, doi: 10.1016/0022-3115(83)90101-0.

[19] J. W. McMurray *et al.*, "Thermodynamic assessment of the oxygen rich U-Ce-O system," *Journal of Nuclear Materials*, vol. 467, pp. 588–600, 2015, doi: 10.1016/j.jnucmat.2015.10.008.

[20] R. C. Belin, M. Strach, T. Truphémus, C. Guéneau, J. C. Richaud, and J. Rogez, "In situ high temperature X-Ray diffraction study of the phase equilibria in the UO_2-PuO_2-Pu_2O_3 system," *Journal of Nuclear Materials*, vol. 465, pp. 407–417, 2015, doi: 10.1016/j.jnucmat.2015.06.034.

[21] M. Strach, "In-Situ Studies Of Uranium-Plutonium Mixed Oxides," 2015.

[22] C. Sari, U. Benedict, and H. Blank, "A study of the ternary system UO_2-PuO_2-Pu_2O_3," *Journal of Nuclear Materials*, vol. 35, no. 3, pp. 267–277, Jun. 1970, doi: 10.1016/0022-3115(70)90211-4.

[23] D. Simeone, P. Garcia, A. Miard, G. Baldinozzi, F. Porcher, and J. Berar, "Phase Separation in Fluorite-Related $U_{1-y}Ce_yO_{2-x}$: A Re-Examination by X-ray and Neutron Diffraction," *Inorg Chem*, vol. 58, pp. 11599–11605, 2019, doi: 10.1021/acs.inorgchem.9b01469.

[24] C. Schreinemachers, G. Leinders, G. Modolo, M. Verwerft, K. Binnemans, and T. Cardinaels, "Fabrication of Nd- and Ce-doped uranium dioxide microspheres via internal gelation," *Journal of Nuclear Materials*, vol. 535, p. 152128, 2020, doi: 10.1016/j.jnucmat.2020.152128.

[25] R. Lorenzelli and B. Touzelin, "Sur le système UO_2-CeO_2; étude cristallographique à haute température," *Journal of Nuclear Materials*, vol. 95, no. 3, pp. 290–302, Dec. 1980, doi: 10.1016/0022-3115(80)90371-2.

[26] T. L. Markin and E. C. Crouch, "Thermodynamic data for U-Ce-oxides," *Journal of Inorganic and Nuclear Chemistry*, vol. 32, no. 1, pp. 77–82, 1970, doi: 10.1016/0022-1902(70)80450-X.

[27] T. B. Lindemer and T. M. Besmann, "Chemical thermodynamic representation of $UO_{2\pm x}$," *Journal of Nuclear Materials*, vol. 130, pp. 473–488, 1985, doi: doi.org/10.1016/0022-3115(85)90334-4.

[28] J. Härtwig, G. Hölzer, E. Förster, K. Goetz, K. Wokulska, and J. Wolf, "Remeasurement of characteristic X-ray emission lines and their application to line profile analysis and lattice parameter determination," *physica status solidi (a)*, vol. 143, no. 1, pp. 23–34, 1994, doi: https://doi.org/10.1002/pssa.2211430104.

[29] J. B. Nelson and D. P. Riley, "An experimental investigation of extrapolation methods in the derivation of accurate unit-cell dimensions of crystals," *Proceedings of the Physical Society*, vol. 57, no. 3, pp. 160–177, May 1945, doi: 10.1088/0959-5309/57/3/302.

[30] R. Jenkins and W. N. Schreiner, "Intensity Round Robin Report," *Powder Diffr*, vol. 4, no. 2, pp. 74–100, Jun. 1989, doi: 10.1017/S0885715600016456.

[31] J. K. Fink, "Thermophysical properties of uranium dioxide," *Journal of Nuclear Materials*, vol. 279, no. 1, pp. 1–18, Mar. 2000, doi: 10.1016/S0022-3115(99)00273-1.

[32] R. Venkata Krishnan *et al.*, "Synthesis, characterization and thermal expansion measurements on uranium-cerium mixed oxides," *Journal of Nuclear Materials*, vol. 414, no. 3, pp. 393–398, 2011, doi: 10.1016/j.jnucmat.2011.05.010.

[33] A. C. Tas and M. Akinc, "Cerium Oxygen Apatite ($Ce_{4.67}[SiO_4]_3O$) X-Ray Diffraction Pattern Revisited," *Powder Diffr*, vol. 7, no. 4, pp. 219–222, Dec. 1992, doi: 10.1017/S0885715600018753.

[34] Ahmet Cuneyt Tas, "Phase relations in the system CeO_2-Al_2O_3-SiO_2 in inert and reducing atmospheres," Iowa State University, 1993.

[35] C. Schreinemachers, G. Leinders, G. Modolo, M. Verwerft, K. Binnemans, and T. Cardinaels, "The conversion of ammonium uranate prepared via sol-gel synthesis into uranium oxides," *Nuclear Engineering and Technology*, vol. 52, no. 5, pp. 1013–1021, 2020, doi: 10.1016/j.net.2019.11.004.

[36] C. Schreinemachers *et al.*, "Structural changes of Nd- and Ce-doped ammonium diuranate microspheres during the conversion to $U_{1-y}Ln_yO_{2\pm x}$," *Journal of Nuclear Materials*, vol. 542, p. 152454, Dec. 2020, doi: 10.1016/j.jnucmat.2020.152454.

[37] J. L. COLLINS, M. H. LLOYD, and R. L. FELLOWS, "The Basic Chemistry Involved in the Internal-Gelation Method of Precipitating Uranium as Determined by pH Measurements," *Radiochim Acta*, vol. 42, no. 3, pp. 121–134, Jun. 1987, doi: 10.1524/ract.1987.42.3.121.

[38] V. N. Vaidya, S. K. Mukherjee, J. K. Joshi, R. V. Kamat, and D. D. Sood, "A study of chemical parameters of the internal gelation based sol-gel process for uranium dioxide," *Journal of Nuclear Materials*, vol. 148, no. 3, pp. 324–331, May 1987, doi: 10.1016/0022-3115(87)90026-2.

[39] C. Schreinemachers *et al.*, "Hydrolysis of Uranyl-, Nd-, Ce-Ions and their Mixtures by Thermal Decomposition of Urea," *Eur J Inorg Chem*, vol. 2022, no. 4, Feb. 2022, doi: 10.1002/ejic.202100453.

[40] W. Tian, M. A. A. Pouchon, H. Guo, D. Chen, X. Yin, and Z. Qin, "Fabrication of CeO_2 ceramic spheres as a surrogate of nuclear fuel by an improved microwave-assisted rapid internal gelation process," *Ceram Int*, vol. 44, no. 6, pp. 6739–6746, Apr. 2018, doi: 10.1016/j.ceramint.2018.01.090.

[41] P. Yu, S. A. Hayes, T. J. O. Keefe, M. J. O. Keefe, and J. O. Stoffer, “The Phase Stability of Cerium Species in Aqueous Systems and Pourbaix Diagram Calculations,” *J Electrochem Soc*, vol. 153, no. C74, 2006, doi: 10.1149/1.2130572.

[42] E. Rocchini *et al.*, “Relationships between structural/morphological modifications and oxygen storage-redox behavior of silica-doped ceria,” *J Catal*, vol. 194, no. 2, pp. 461–478, 2000, doi: 10.1006/jcat.2000.2954.

[43] H. A. M. van Hal and H. T. Hintzen, “Compound formation in the Ce_2O_3-SiO_2 system,” *J Alloys Compd*, vol. 179, no. 1–2, pp. 77–85, Feb. 1992, doi: 10.1016/0925-8388(92)90207-P.

[44] A. C. Tas and M. Akinc, “Phase Relations in the System Ce_2O_3–$Ce_2Si_2O_7$ in the Temperature Range 1150° to 1970°C in Reducing and Inert Atmospheres,” *Journal of the American Ceramic Society*, vol. 77, no. 11, pp. 2953–2960, 1994, doi: 10.1111/j.1151-2916.1994.tb04530.x.

[45] G. Colak, G. Leinders, J. Vleugels, R. Delville, and M. Verwerft, “Improved doping and densification of uranium oxide microspheres using starch as pore former,” *Journal of Nuclear Materials*, vol. 577, p. 154319, 2023, doi: 10.1016/j.jnucmat.2023.154319.

[46] H. Cao *et al.*, “Differential interplay between Ce and U on local structures of $U_{1-x}Ce_xO_2$ solid solutions probed by X-ray absorption spectroscopy,” *Journal of Nuclear Materials*, vol. 515, pp. 238–244, 2019, doi: 10.1016/j.jnucmat.2018.12.042.

[47] A. Örn, “Degradation studies on polydimethylsiloxane,” Åbo Akademi University, 2019.

[48] R. J. Hamilton, “Hydrolysis of Silicone Polymers in Aqueous Systems,” Lakehead University Hydrolysis, 2001.

[49] G. Ducom, B. Laubie, A. Ohannessian, C. Chottier, P. Germain, and V. Chatain, “Hydrolysis of polydimethylsiloxane fluids in controlled aqueous solutions,” *Water Science and Technology*, vol. 68, no. 4, pp. 813–820, 2013, doi: 10.2166/wst.2013.308.

[50] G. Palmer, “Volatilization of Refractory Silica in Hydrogen Water Vapour Gas Streams,” *Worldforum Technology Trends*, vol. 4, no. 4, pp. 63–70, 2012, [Online]. Available: https://www.refractories-worldforum.com/php/paper_download.php?article_id=100206&hash=b4882f5842

[51] R. D. Hunt, G. W. C. M. Silva, T. B. Lindemer, K. K. Anderson, and J. L. Collins, “Preparation of uranium fuel kernels with silicon carbide nanoparticles using the internal gelation process,” *Journal of Nuclear Materials*, vol. 427, no. 1–3, pp. 245–248, 2012, doi: 10.1016/j.jnucmat.2012.04.027.

[52] R. D. Hunt, J. L. Collins, and B. S. Cowell, “Use of boiled hexamethylenetetramine and urea to increase the porosity of cerium dioxide microspheres formed in the internal gelation process,” *Journal of Nuclear Materials*, vol. 492, pp. 1–5, 2017, doi: 10.1016/j.jnucmat.2017.04.061.

[53] R. D. Hunt, J. L. Collins, M. H. Lloyd, and S. C. Finkeldei, “Production of more ideal uranium trioxide microspheres for the sol-gel microsphere pelletization process without the use of carbon,” *Journal of Nuclear Materials*, vol. 515, pp. 107–110, 2019, doi: 10.1016/j.jnucmat.2018.12.029.

[54] J. L. Collins *et al.*, “Trichloroethylene replacements for the cleaning of silicone oil used in the internal gelation process,” *Journal of Nuclear Materials*, vol. 558, p. 153379, Jan. 2022, doi: 10.1016/j.jnucmat.2021.153379.

[55] IAEA, “IAEA TECDOC 352 - Advanced fuel technology and performance,” 1985.

[56] C. M. Sempere, C. J. M. Civera, C. Cozzo, S. Vaucher, and M. A. Pouchon, “Innovative production of nuclear fuel by microwave internal gelation: Theoretical microwaves-microspheres interaction,” 2011.

[57] M. Cabanes-Sempere, C. Cozzo, S. Vaucher, J. M. Catalá-Civera, and M. A. Pouchon, “Innovative production of nuclear fuel by microwave internal gelation: Heat transfer model of falling droplets,” *Progress in Nuclear Energy*, vol. 57, pp. 111–116, 2012, doi: 10.1016/j.pnucene.2011.12.011.

[58] K. Suresh Kumar, H. P. Nawada, and N. P. Bhat, “Comparative study of thermal decomposition of the sol-gel products of U and Ce by external and internal gelation processes,” *Journal of Nuclear Materials*, vol. 321, no. 2–3, pp. 263–268, 2003, doi: 10.1016/S0022-3115(03)00278-2.